sustainability

MDPI

Article

Intelligent Energy Management System for Mobile Robot

Min-Fan Ricky Lee [1,2,*] and Asep Nugroho [1]

[1] Graduate Institute of Automation and Control, National Taiwan University of Science and Technology, Taipei 106335, Taiwan
[2] Center for Cyber-Physical System Innovation, National Taiwan University of Science and Technology, Taipei 106335, Taiwan
* Correspondence: rickylee@mail.ntust.edu.tw

Abstract: Mobile robots used for search and rescue suffer from uncertain time duration for sustainable operation. Solar energy has the drawback that it fluctuates depending on the weather. By integrating the battery and supercapacitor, the energy management system eliminates this shortcoming. Managing power sharing between the battery and the supercapacitor is conducted by the fuzzy logic controller and proportional integral controller. The fuzzy logic controller provides a reference value to the proportional integral controller to keep the supercapacitor voltage at a certain value. It provides sufficient space to store solar energy and at the same time helps the battery to stay longer for operation. Moreover, the proposed energy management system offers a feature for providing a load power reference recommendation and offers the hibernate mode to save energy when the main power source is too weak, and it is suitable for mobile robot application. The simulation and experiment show that the energy management system design maintains the supercapacitor voltage and regulates the power sharing. Moreover, it also provides a percentage power reference recommendation for the central controller to manage its load current. It reduces the battery power consumption up to 35% and reduces peak current up to 5%, depending on the existing photovoltaic current and load management.

Keywords: sustainable energy; energy management system; mobile robot; supercapacitor; fuzzy logic

Citation: Lee, M.-F.R.; Nugroho, A. Intelligent Energy Management System for Mobile Robot. *Sustainability* **2022**, *14*, 10056. https://doi.org/10.3390/su141610056

Academic Editors: Wenliang Zhou and Peng Yang

Received: 10 May 2022
Accepted: 4 August 2022
Published: 14 August 2022

1. Introduction

The search and rescue task (SAR) is rapidly increasing in line with the increasing number of accidents involving human mobility. The SAR task has difficulties such as potential hazards, large covered area, and task complexity. It could lead to risk for the SAR team, so in recent years, mobile robots (MR) have been employed in SAR operation [1]. The operation time duration is flexible depending on the large covered area and task complexity, so the energy management system (EMS) has a primary role in keeping MR alive during the mission [2]. Generally, EMS is needed if the system has multiple power sources and it consists of a primary power source, secondary power source, energy storage, and power controller [3]. The continual and non-interruptible power is supplied by the primary power source such as a battery or fuel cell, whereas the secondary power source is used for the extended state of charge (SoC) battery life [4].

In the physical layer, EMS could be constructed by the battery, supercapacitor (SC), and power converter that are usually applied in electric vehicles (EV). This structure is commonly called a hybrid energy storage system (HESS) where the battery behaves as the primary source, whereas the SC performs as temporary storage when the power converter harvests regenerative energy during the EV braking [5]. The benefit of using the SC to store temporary energy is a much longer cycle life and high energy density so that it could release huge energy when the load is excessive. This is beneficial in reducing the abrupt high load that increases battery lifespan [6].

There are four typical topologies of HESS (i.e., passive, semi-active type I, semi-active type II, and fully active). The passive topology does not have a control algorithm and

DC/DC converter. It is the easiest to implement but it does not have a degree of freedom (DOF) to control the current flow. The DC/DC converter regulating the battery current and using the SC as the DC bus is called the semi-active type I. This structure is prone to fluctuation in the DC bus caused by the SC voltage that needs a long time to settle. Whereas the semi-active type II uses a battery as the DC bus and the DC/DC converter is used to regulate the SC current flow. It offers the stability of the DC bus. In this structure, the current load is supplied mainly from the battery, so if the current that is injected by the DC/DC converter is too high, it will be absorbed by the battery. Otherwise, if the current that is injected is too low, it will be backed up by the battery. However, it will produce a large voltage drop in the DC bus when the battery SoC is too low. Finally, the fully active topology uses two DC/DC converters for the SC and the battery. It offers the best DOF of the current flow. However, designing individual controllers for each DC/DC converter is a big challenge and the hardware cost is not cheap [6].

Several HESS topologies were investigated but the majority of them were carried out in EV application and microgrid [3,5–9]. The non-isolated multi-input converters (MICs) to manage energy sharing between the SC and the battery were proposed and tested by using a small EV [3]. The design of the MICs was constructed by using a unidirectional and bi-directional buck-boost converter. There were five switches to control the current flows. Three selectors of modes, proportional integral (PI)-controller, and fuzzy logic controller (FLC) were applied. The first mode was discharging mode, with the current from the SC and battery flowing together to load. The second mode was charging/discharging mode; it occurred when the battery charged the SC and at the same time supplied the battery current to the load. The last mode was regenerative; it was applied to take energy from regenerative braking of EV to store in the SC. The FLC and PI-controller were used to manage how much power they want to allocate. This idea to use FLC and PI-controller can be adopted as a reference for designing a control scheme because it promises good performance without too much effort.

The EMS for a residential consumer installation was proposed by [8]. By combining the photovoltaic (PV) system, the SC, and the battery on a large scale, it was difficult to always estimate the SC SoC and battery accurately. They proposed an equation to find the relationship between the SC SoC and its voltage. Although the equation result was just an approximate value, it was useful to reduce complexity for estimating the SC SoC.

There are slight issues with the EMS applied in MR that is studied in [4,10–13]. The UAV's EMS proposed by [2] was constructed with an independent DC/DC converter for each power source and the outputs are connected together to DC link as the main grid. It is categorized as a fully active topology. Because it does not use SC, the energy from PV cannot be stored longer in the DC grid. The topology is also high-cost and not easy to control. In this structure, it uses the PI-controller to control the bi-directional converter with the DC voltage as the feedback control.

Several control algorithms such as rule-based [14], FLC [3,15–17], filtering [18], model predictive control (MPC) [19], and neural network (NN) [20] have been investigated. The MPC and NN offered an optimum solution. However, it is not easy to provide a large dataset to train the NN model. Another problem is accuracy depending on the quality of data. The MPC is prone to a mismatch in the mathematical model if some parameters are not enough to consider, and it is difficult to mathematically model for each power source. For real-time application, FLC has advantages, i.e., it is easy to logically understand and it is not too much depending on the mathematical model [6].

Although the research in [2] had some drawbacks, the idea is good as the foundation to design EMS. Changing the topology from a fully active topology to the semi-active type II and giving a little bit of structure modification can reduce some of the drawbacks. Based on a trade-off between hardware cost and complexity control algorithm, the semi-active type II is the best matched to use in the MR.

This paper attempted modification of the topology proposed in [2] and the control scheme in [3,6] so that it can be matched for the MR application. The primary contribution

of this paper was to propose two control schemes for power sharing and load power recommendation. This study also removes the SC SoC as an input of FLC so it could simplify the computation process but it also did not lose performance significantly. Moreover, this study offered an important ability for MR (i.e., to provide sustainable power during the operation). It would extend the mission duration when operating the MR.

The paper is composed as follows. Section 2 reviews the component modelling and describes hardware and software implementation. Section 3 explains the results and provides the discussion. Finally, Section 4 discloses our conclusion.

2. Materials and Methods

2.1. Modelling

Before designing the EMS for MR, one must consider what kind of energy one wants to harvest. Typically, energy can be harvested from nature, i.e., solar, wind, and vibration energy. For MR, only solar and vibration energy can be easily gathered. The wind needs enough height to rotate the wind generator. Whereas the energy density of the piezoelectric transducer is too small, practically only 19 mW/cm^3 [21]. In the commercial market, the PV panel can convert solar energy with efficiency up to 20%. It is promising to choose solar energy as a secondary power source.

2.1.1. PV Modelling

Figure 1 is a representation of the equivalent circuit model of PV used by [22]. Based on Kirchhoff Current Law (KCL), I_{ph} can be defined as in (1) and the current which flows in the diode can be expressed as in (2), where I_{PV}, I_{ph}, I_{rs}, V_{PV}, n, K, T, and q are output current of PV (A), approximate short-circuit current of PV (A), reverse saturation current (A), output voltage of PV (V), the diode-ideality factor, Boltzmann constant 1.3806×10^{-23} J/K, temperature of the P-N junction (K), and electron charge 1.6021×10^{-19} C, respectively. Whereas R_s and R_p are parasitic resistance (Ω).

$$I_{PV} = I_{ph} - \frac{V_d}{R_p} - I_d, \tag{1}$$

$$I_d = I_{rs}\left(e^{\frac{q(V_{PV}+I_{PV}R_S)}{nKT}} - 1\right), \tag{2}$$

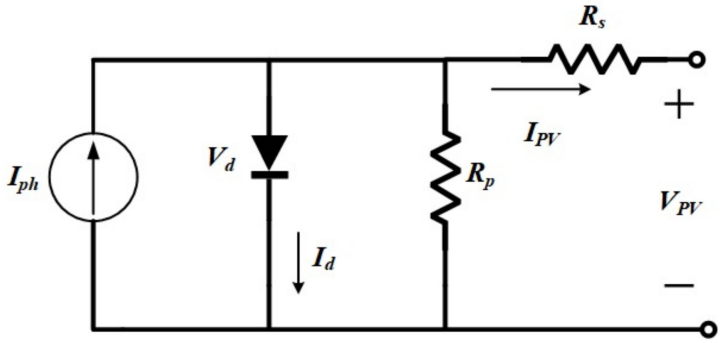

Figure 1. The equivalent circuit model of PV.

By simplification, the reverse saturation current I_{rs} is expressed, as in (3) and (4). Whereas E_g, I_{rs_ref}, and T_{ref} are activation energy, reverse saturation current, and temperature at standard test conditions/STC (25 °C), respectively. It is clear that PV has a non-linear current source behavior, whereas most DC-DC power converters are designed with an assumption that the input is a constant voltage source. This leads the DC power converter to find it difficult to achieve stability because the PV cannot provide a constant voltage. To

solve that problem, usually the PV energy is stored in the capacitor before deliverance to the load/battery.

$$I_{PV} = I_{ph} - \frac{V_{PV} + I_{PV}R_S}{R_p} - I_{rs}\left(e^{\frac{q(V_{PV}+I_{PV}R_S)}{nKT}} - 1\right), \tag{3}$$

$$I_{rs} = I_{rs\_ref}\left(\frac{T}{T_{ref}}\right)^3 e^{\frac{qE_g}{nK(\frac{1}{T}-\frac{1}{T_{ref}})}}, \tag{4}$$

The MPPT has a crucial role in gathering small energy from PV, but it does not guarantee always tracking the optimum point because non-linearity PV behavior depends on several factors such as irradiance, temperature, type of serial-parallel connection, and partial shading.

2.1.2. SC Modelling

The two resistor-capacitor (RC) branch circuits for the SC model are shown in Figure 2. It can be separated into the main cell, slow cell, and loss function [23]. By KCL, I_{SC} can be obtained, as in (5), and the main cell C_1, as in (6). It should be noted that R_f, R_1, and R_2 denote parasitic resistance in the loss cell, main cell, and slow cell, respectively. Whereas C_o and C_V are constant capacitance (F) and variable capacitance depending on V_1. The I_{rf} is current that flows into R_f, and by neglecting I_{rf}, the V_{SC} becomes (7).

$$I_{SC} = I_1 + I_2 + I_{Rf} \tag{5}$$

$$C_1 = C_o + C_V V_1 \tag{6}$$

$$V_{SC} = N_S\left(V_1 + R_1\frac{I_{SC}}{N_P}\right) \tag{7}$$

where V_{SC} and I_{SC} are voltage and current of the SC pack, respectively. N_S and N_P are the number of series and parallel branches of the SC connections, respectively. By paralleling the SC, it not only increases the capacitance, but also increases I_{SC}. This must be considered in designing the DC/DC converter; otherwise, it will lead to inrush current that can damage the power converter. The electric charge (Q_1) and its voltage (V_1) are expressed as in (8).

$$V_1 = \frac{-C_o \pm \sqrt{C_o{}^2 + 2C_V Q_1}}{C_V}, \tag{8}$$

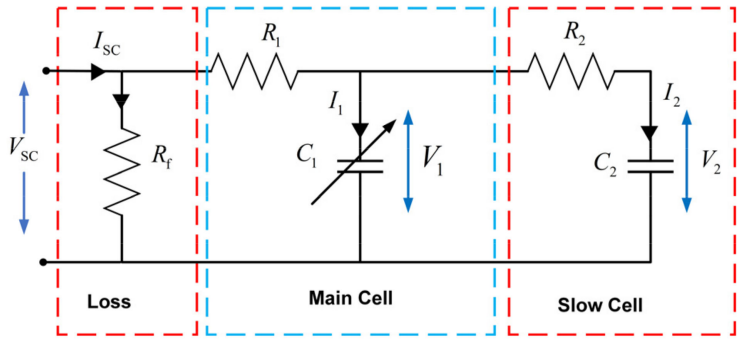

Figure 2. The equivalent circuit model of SC.

It can be concluded that in the beginning the SC can charge or discharge a large current, then it will decrease gradually in line with the decrease of $V_1 - V_2$. Moreover, the SoC_{SC} can be expressed by (9) [24].

$$SoC_{SC}(t) = \frac{C_{SC}V_{SC\_init(t=0)} - \int_0^t I_{SC}\,d\tau}{Q_S}, \tag{9}$$

where C_{SC}, I_{SC}, V_{SC} (t), V_{SC_init}, Q_S, and τ are SC capacitance value (F), SC charge/discharging current (A), current SC voltage (V), initial SC voltage (V), supercapacitor rated charge (C), and RC-time constant, respectively. It is clear that SoC_{SC} is almost linearly in line with its voltage. By maintaining its voltage, the SoC_{SC} can be kept at a certain level. In a real implementation, observing V_{SC} is cheaper to implement with a low-cost voltage sensor rather than using a current sensor.

2.1.3. Battery Modelling

The second RC model battery is shown in Figure 3. The representation of the model is expressed, as in (10) and (11), where R_s is the internal equivalent series resistance of battery, while R_{p1} and R_{p2} are the internal equivalent parallel resistance [25]. On the other hand, the V_{OCV}, C_1, and C_2 are battery open circuit voltage, internal capacitance parasitic RC-network 1, and capacitance parasitic RC-network 2, respectively.

$$V_{Bat} = V_{OCV}(SoC) + I_{Bat}R_s + V_{C_1} + V_{C_2}, \tag{10}$$

$$V_{Bat} = V_{OC}(SoC) + I_{Bat}R_s + I_{Bat}\left(R_{p1}e^{\frac{t}{\tau_1}} + R_{p2}e^{\frac{t}{\tau_2}}\right), \tag{11}$$

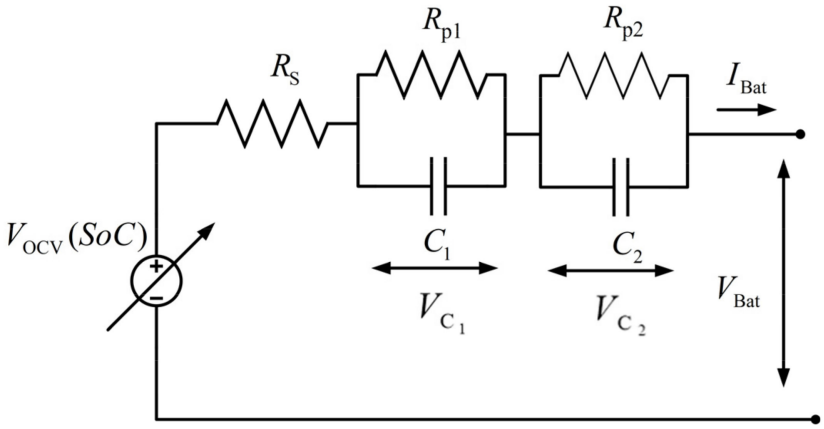

Figure 3. The equivalent circuit of battery.

Estimating SoC of battery is not easy because the accuracy depends on several factors such as chemical characteristics, temperature, profile of current charge/discharging, and age of battery. Internal resistance R_S and two RC-network parameters must be identified accurately. For accurate results, one must investigate the use of impedance spectroscopy [26]. The common algorithm to estimate SoC is Coulomb Counting (CC) with discrete computation trapezoidal rule as in (12) and (13).

$$SoC(t) = SoC_0 - \frac{1}{C_n}\int I_{Bat} \tag{12}$$

$$SoC(k) = SoC_0 - \frac{1}{C_n}\left(\Delta t \times \frac{I_{Bat}(k) + I_{Bat}(k-1)}{2}\right) \tag{13}$$

where $SoC(t)$, SoC_0, and k are the current SoC, initial SoC, and a sequence index of data, respectively. C_n and I_{Bat} are the battery capacity (Ah) and the charge/discharge current. The CC accuracy depends on the rapidity of time sampling (Δt) and current sensor precision. Based on [27], the drawbacks of the CC are error propagation and requiring the high-speed and high-precision current sensor. When the initial SoC (SoC_0) is not correct or the current sensor measurement is not valid, it will be accumulated by the integrator.

In designing EMS, estimation of SoC is one of the crucial tasks because it determines the limit of the remaining battery capacity that must detach from the load to prevent over-discharging. Because the battery shows complex nonlinear behavior, characterization is

needed for building an accurate model. The impedance spectroscopy produces accurate parameter estimation but it is high-cost laboratory equipment. The common characterization to find the battery parameter is pulse discharge. The first step is to charge the battery until full charge and then the battery is discharged with constant current 0.5 or 1 C-rate. After that, one must disconnect the battery and take a rest for around 1 h, and then record the voltage. One must repeat the procedure until the battery is fully depleted. This will create a curve SoC-V_{OCV}, where V_{OCV} is the battery terminal voltage when it is not connected to the load or charger.

2.2. Intelligent EMS

There are three aspects that must be considered in the design of the proposed EMS. First, we had to decide the proper MPPT. It was crucial to optimize the harvesting PV energy. Second, the choice of the switching mode was related to how to reduce switching losses in the power converter. Third, the choice of topology was very crucial because it had some trade-offs such as cost, complexity control system, and performance. In addition, the choice of topology also determined which control scheme was suitable.

2.2.1. MPPT

Giving the ability to harvest energy from nature is one feature that is offered by this study. To maximize the harvesting of solar energy, the MPPT had a crucial role and the basic idea of the MPPT was to control the PV voltage such that the value of dP/dV was approximately equal to zero and it was important to ensure autonomous mobile robots to obtain optimum energy from solar irradiance [28]. When dP/dV was less than zero, this means that the PV output voltage was not enough to deliver its current, so it needed to boost the PV voltage. The relationship between power and voltage is shown in Figure 4. Unfortunately, the maximum point was always changed depending on temperature and irradiance, so it was very difficult to always track properly. Moreover, sometimes it also created multiple peak points that led to the local minimum trap.

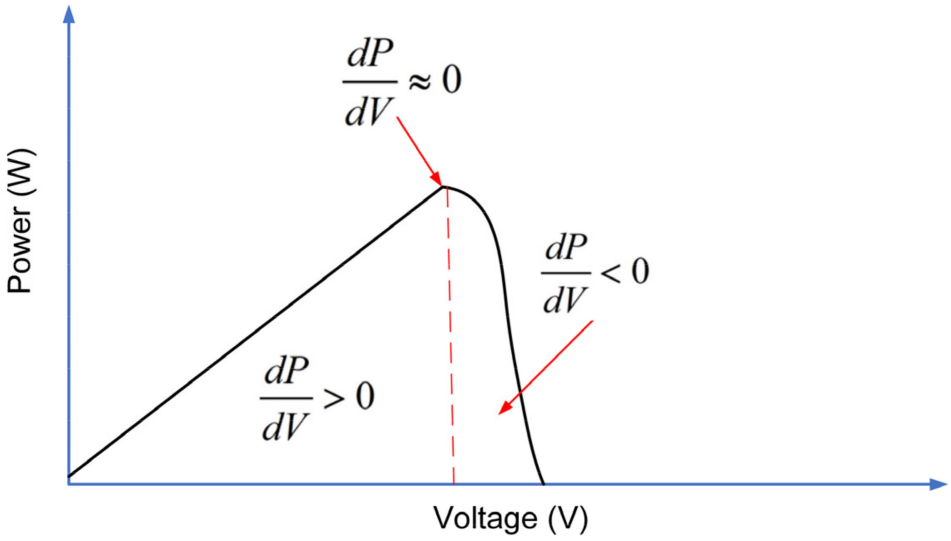

Figure 4. The power-voltage curve of PV.

The classical algorithm Perturb and Observe (P&O) was very cheap to implement because it was already integrated into the IC boost controller. The P&O algorithm was quite simple; when dP/dV was greater than zero, the MPPT started increasing the pulse width modulation (PWM) duty cycle to drive the boost converter, and at the same time, it monitored the PV output power until dP/dV decreased to approximately zero. After reaching the maximum point, the controller would lock the duty cycle.

2.2.2. The Burst Switching Pattern

For low input voltage and low power applications, the conduction and switching losses of the power converter were considered. The conduction loss was caused by parasitic resistance of the inductor and switching device (Metal Oxide Semiconductor Field Effect Transistor/MOSFET). Switching loss was led by how fast the on-off transition occurred at MOSFET. The conduction (P_{ON}) and switching loss (P_{Sw}) were expressed, as in (14) and (15), where $R_{ds\,(ON)}$ is the value of drain-source on-resistance MOSFET. Whereas t_r and t_f are the rise and fall time when MOSFET turned on/off, respectively. Finally, f_{Sw} is the switching frequency of the power converter. The form of burst switching pattern is shown in Figure 5.

$$P_{ON}(t) = {I_{Load}}^2 \times R_{ds\,(ON)} \times \frac{V_o}{V_S}\ (W) \tag{14}$$

$$P_{Sw}(t) = \frac{1}{2} \times V_S \times I_{Load} \times \left(t_r + t_f\right) f_{Sw} \tag{15}$$

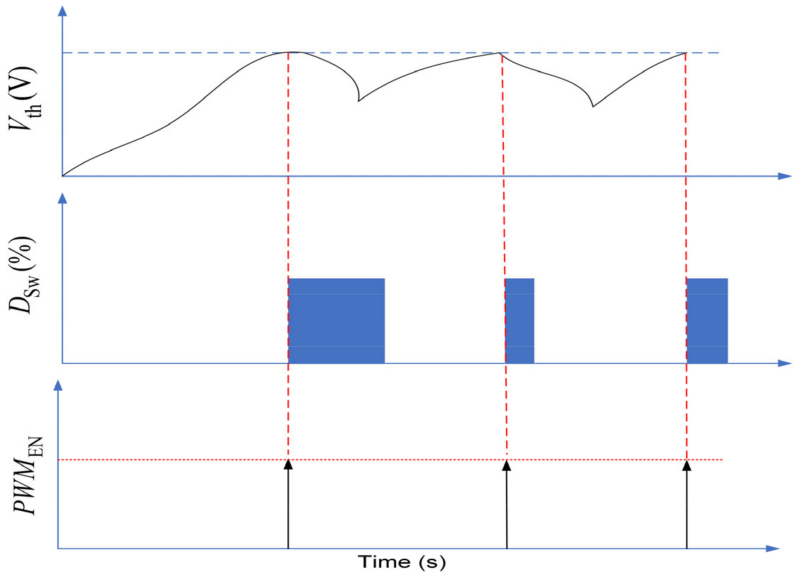

Figure 5. The burst mode switching pattern.

Dealing with switching loss, the burst mode switching pattern was proposed by [29]. This is unlike a conventional boost converter that was operated in continuous time. In the burst mode, the clock generator provided PWM and at the same time, it monitored the input voltage. The duty cycle of boost converter (D_{Sw}) was only enabled (PWM_{EN}) when the input voltage reached the minimum voltage threshold V_{th}. It drastically reduced the switching loss. However, because it was not operated continuously, it caused a large fluctuation in the output side. This idea was only suitably adopted when the semi-active type II was used as topology, and in the EMS where a battery was treated as the DC bus.

2.2.3. The Semi-Active Type II HESS

The topology proposed by [2] was adopted in this paper with some adjustments that are displayed in Figure 6. The primary modification was to move the DC link connected parallel with the battery and load and it would change from a fully active topology to the semi-active type II. The bi-directional and unidirectional boost converters were used in [2], whereas this paper only used a unidirectional boost converter. The disadvantage of method [2] is the hardware cost and the fact that it is not easy to design the PI-controller for the bidirectional boost converter, and it causes large losses when it is used too often.

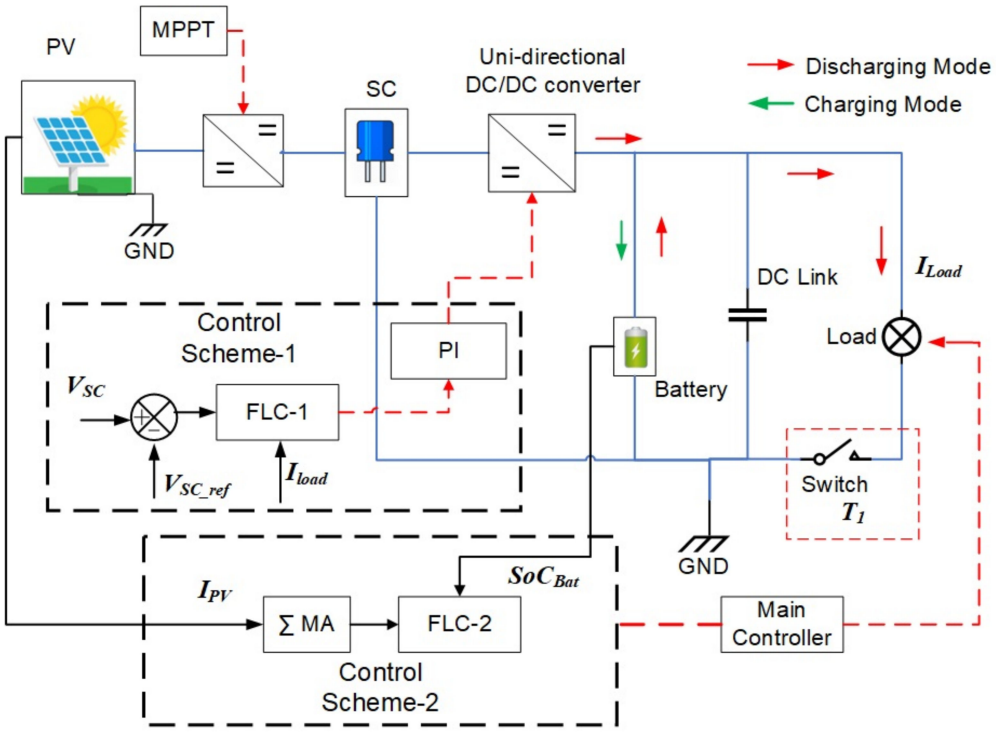

Figure 6. The proposed EMS block diagram.

On the other hand, a series of one-way power flow offers fewer switching losses because the unidirectional DC/DC converter was only used when the voltage of SC was sufficient to deliver energy into the battery/load. In this study, the energy from PV was not directly transferred to the battery but it was dumped into the SC. Low internal resistance and no internal voltage source made the SC ideal to store energy temporarily because it provided sufficient difference in the voltage between PV and the SC. The reason to use a series of one-way power flow was to reduce the over-usage of DC/DC converter that led to large switching losses.

Two different control schemes were implemented. The control scheme-1 was focused on controlling power sharing between the SC and battery. While the control-2 scheme was only focused on giving recommendations as to how much percentage of the power could be consumed so the main controller would arrange which sensor or actuator was given priority. The decision-making related to load management was fully determined by the main controller. Every mission had a different goal, so the sensor or actuator that was given priority might be different for each mission.

For example, if the mission in the field has a lot of obstacles, while the ultrasonic sensor/Lidar consumes much energy, the main controller would choose to keep it alive and would choose to turn off another unnecessary sensor such as a temperature infrared sensor. The reference also could be used to determine the task. For instance, if the percentage of the power reference was too low, the main controller could consider changing into hibernate mode or returning to base rather than continuing the mission.

To prevent over-discharge of battery that could cause the MR failure to complete the operation, the switch (T_1) had an important role in detaching the battery and load, then initiating the battery charging mode that is called hibernate mode. In the real mission, harvesting PV energy could still sometimes not be enough to energize the robot completing the mission. However, at least an emergency report could be sent to the base station.

Figure 7 is the equivalent circuit of the proposed EMS topology. It is a series path of connection between the SC and battery which is regulated by a unidirectional boost converter. There are two boost converters. The boost converter 1 is driven by MPPT IC and the load switch T_1 and the boost converter 2 is driven by low-cost microcontroller.

The two FLC from control schemes-1 and 2 that are described in Figure 6, were both implemented in a computer.

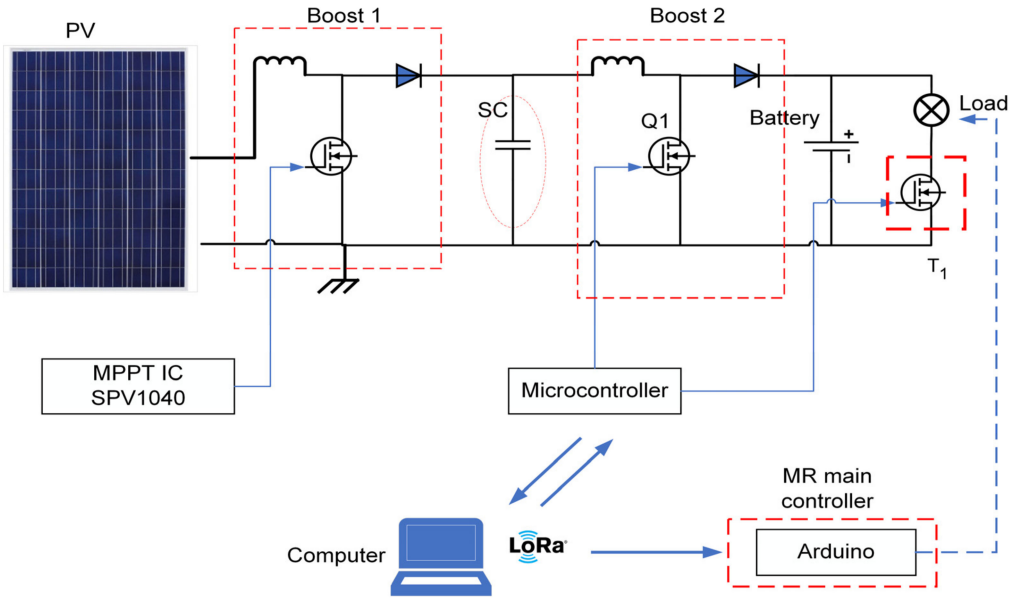

Figure 7. The equivalent circuit of proposed EMS.

LoRa was one of the low-power wireless data communication devices that were available in the market; however, if over-used to transmit the data, it would consume a great deal of power. Based on its datasheet, it consumed 106 mA when transmitting data and 15 mA when receiving data. The total power consumption for the whole system could be estimated as follows in Table 1. One must assume that the total current consumption for the whole system required around 3.26 watt. In this case, the PV module had to produce more than 3.36 watt to obtain benefits of the EMS.

Table 1. Estimating hardware power consumption.

Specifications	Value
LoRa Module	121 mA
Controller dsPIC33FJGS502 board	160 mA
Boost converter-1 losses (parasitic at inductor, capacitor, and MOSFET)	70 mA
Boost converter-2 losses (parasitic at inductor, capacitor, and MOSFET)	90 mA
Total	441 mA

Figure 8 explains the FLC-1 and PI-controller proposed for control scheme 1 that was used for controlling power sharing between the battery and the SC. In the first stage, the battery state of charge (SoC_{Bat}) was monitored to determine the mode. It started to disconnect the load when the SoC_{Bat} was less than 20%, which is called discharging/hibernation mode. Vice versa, it was powering the load when SoC_{Bat} was larger than 20% to secure the battery from over-discharging. In the next step, the FLC-1 would arrange how much power must be taken from the SC. The SC current reference ($I^*_{SC\_ref}$) that was arranged by the FLC-1 was utilized as a reference to the PI controller, as in (16). Whereas K_p, K_i, e, and Δt were the proportional coefficient, integral coefficient, error, and time sampling, respectively.

$$u(k) = K_p \cdot e(k) + K_i \sum_{k=1}^{n} e_k \Delta t \quad (16)$$

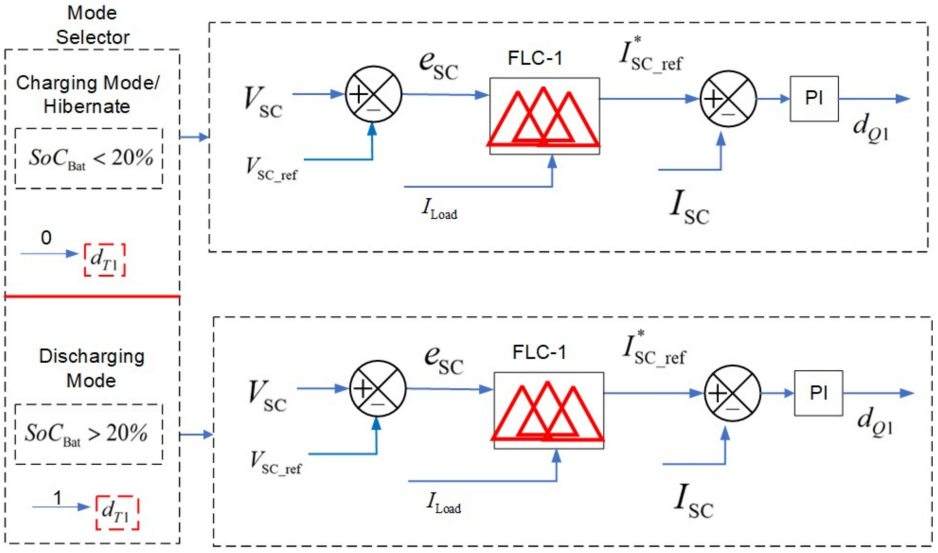

Figure 8. The FLC-1 at control scheme 1.

Two inputs, i.e., output current load (I_{Load}) and e_{SC}, had a role as the FLC input, where e_{SC} was the error between current SC voltage (V_{SC}) and reference SC voltage (V_{SC_ref}). Theoretically, the V_{SC_ref} was expressed as in (17).

$$V_{SC\_ref} = (0.15 - 0.5)V_{mpp} \tag{17}$$

where V_{mpp} was maximum voltage when the PV power was in the peak point. At the peak power, assume V_{mpp} equal to V_{SC_max} so it was multiplied by a factor around 0.15 to 0.5, then it locks the SC SoC (SoC_{SC}) around 15% to 50%. This calculation assumes that SoC_{SC} was in line with its V_{SC}. The rationale to keep the SoC_{SC} at that level was to offer enough differential voltage so that the PV current could flow easily. On the other hand, if SoC_{SC} was fully depleted, it could not help the battery to reduce the peak current load. Simplifying the calculation might lead to a drop in SC voltage after discharging its current because the SC current (I_{SC}) was not already settled at the slow cell of SC. In [8], (18) and (19) were proposed to guarantee that the SC voltage could not be dropped after its current discharge.

$$SoC_{SC} = \frac{1}{3}\left[4\left(\frac{V_{SC\_ref}}{V_{nom}}\right)^2 - 1\right] \tag{18}$$

$$V_{SC\_ref} = \sqrt[2]{\frac{(3 \times SoC_{SC} + 1){V_{nom}}^2}{4}} \tag{19}$$

If one assumes nominal SC voltage (V_{nom}) in line with V_{mpp}, in order to obtain SoC_{SC} equal to 15%, the V_{SC_ref} should be equal to 3 V. Despite the fact that it gave a guarantee for no drop in the SC voltage, in the real case, it took too long to wait to achieve the higher V_{SC_ref}, so it could not quickly help the battery during a heavy load condition. The drop in SC voltage was still acceptable if it was not less than the input boost converter minimum requirement.

Figure 9a,b show triangular and trapezoidal membership functions representing the input FLC-1. The input e_{SC} had five membership functions, i.e., Negative Big (NB), Negative Small (NS), Zero (Z), Positive Small (PS), and Positive Big (PB). Figure 10 represented the membership function of the output FLC-1. As noted, the input I_{Load} and output $I^*_{SC\_ref}$ had four membership functions, i.e., Zero (Z), Small (S), Big (B), and Very Big (VB). Input and output were regulated by several rule base systems defined in Table 2. The Mamdani implication was used to determine the relationship between two input variables i.e., I_{Load} and e_{SC}, as in (20).

$$A \Rightarrow B = A \wedge B = min\,[\mu_A(\ I_{Load}\ ),\ \mu_B\ (\ e_{SC}\ )], \tag{20}$$

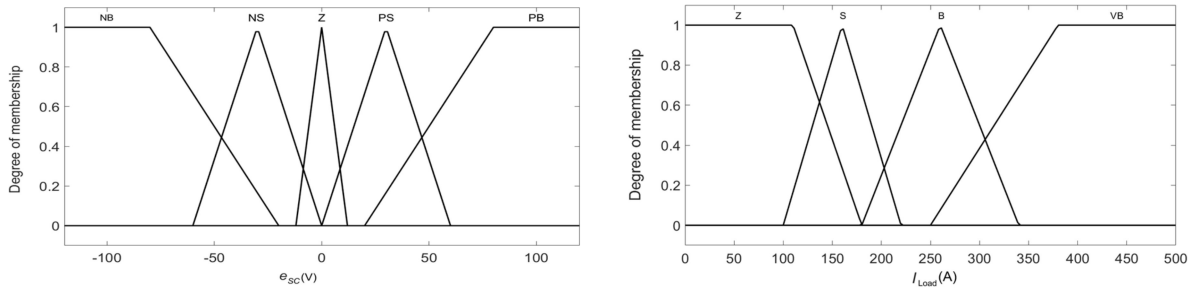

(**a**) (**b**)

Figure 9. Membership function of inputs FLC-1 as: (**a**) error voltage of capacitor (e_{SC}); (**b**) load current (I_{Load}).

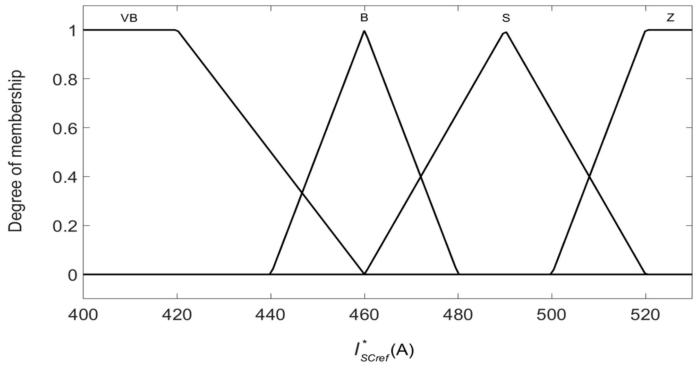

Figure 10. Membership function of output FLC-1 ($I^*_{SC\_ref}$).

Table 2. Rule base of FLC-1.

Rule Base					
					I_{Load}
		Z	S	B	VB
e_{SC}	NB	Z	Z	Z	Z
	NS	Z	Z	Z	Z
	Z	Z	Z	Z	Z
	PS	B	B	VB	VB
	PB	B	B	VB	VB

Finally, the centroid defuzzification was used for calculation of the SC current reference ($I^*_{SC\_ref}$), as in (21). The main goal was keeping V_{SC} at a certain level although the load and PV input current were changing so that the output FLC was more sensitive in relation to e_{SC}. In this case, if the e_{SC} is less than or equal to zero, the $I^*_{SC\_ref}$ would be pushed at zero value. In that condition, the PI-controller would just wait until the FLC reaches a positive value. This ensured that the V_{SC} had enough voltage to deliver its power. To prevent excessive value of the PWM duty cycle, a saturation block was added at the PI-controller.

$$X_{centroid} = \frac{\sum_i \mu(x_i) x_i}{\sum_i \mu(x_i)} \tag{21}$$

Figure 11 was the FLC-2 for calculating percentage of the power reference that would be sent to the main controller. It had two inputs i.e., SoC_{Bat} and the moving average (MA) of I_{PV}. The MA indicated the trend of harvesting energy. If it had a large value, this means the main controller could take more power to energize the load. On the other hand, the SoC_{Bat}

also was considered as a constraint. If the SoC_{Bat} started to decrease quickly, the FLC-2 would start giving reference to the decrease of the load power. This created balancing between reserve energy and load consumption.

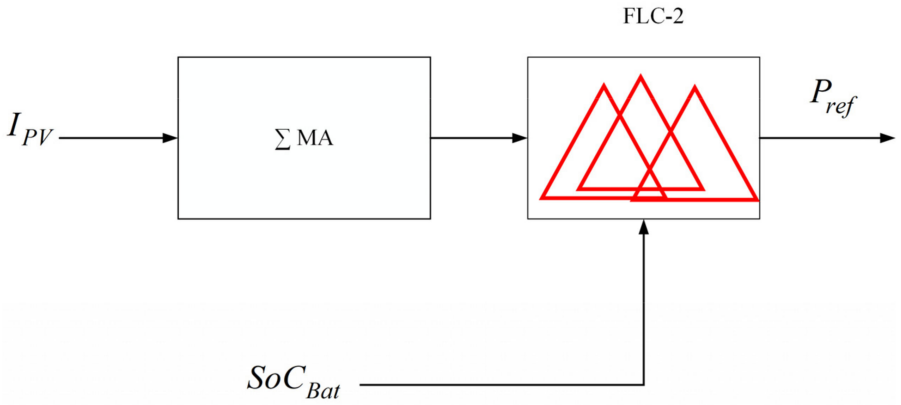

Figure 11. The FLC-2 at control scheme 2.

Sigmoid, Gaussian, and triangle forms were used to represent membership function of input FLC-2, as shown in Figure 12. The input I_{PV} and SoC_{Bat} had three membership functions, i.e., Low (L), Medium (M), and High (H) with the Sigmoid and Gaussian form. The output, i.e., percentage of the power reference, is represented in Figure 13. The relationship between input and output FLC-2 was determined by the rule base that is shown in Table 3.

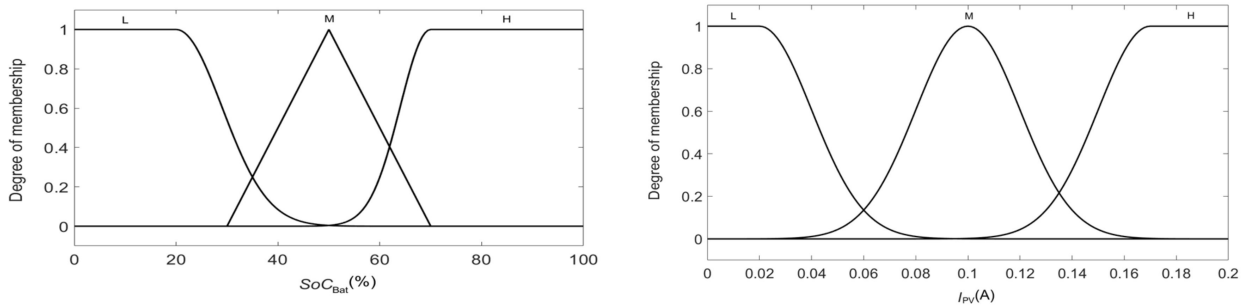

(**a**) (**b**)

Figure 12. Membership function of inputs FLC-2 as: (**a**) SoC battery (SoC_{Bat}); (**b**) moving average (MA) I_{PV}.

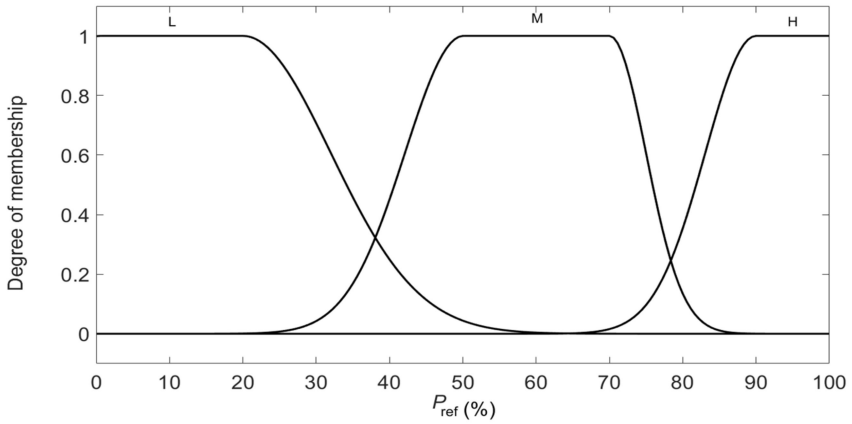

Figure 13. Membership function of output percentage power load (P_{ref}).

Table 3. Rule base of FLC-2.

Rule Base				
		(MA) I_{PV}		
		L	M	H
SoC_{Bat}	L	L	L	L
	M	M	M	H
	H	H	H	H

2.2.4. Hardware and Software Implementation

Designing a power converter for EMS should consider how much power it is desired to regulate. It always has a trade-off i.e., cost, efficiency, and complexity. For low power and low voltage, usually non-isolated topology such as buck, boost, buck-boost, and SEPIC converter is used. The basic calculation of boost converter is expressed, as in (22)–(24):

$$D_{boost} = 1 - \frac{V_{in}}{V_{out}} \tag{22}$$

$$L_{Crit} > \frac{D \times V_{\text{in}}}{2 \times f \times I_{\text{Load}}} \tag{23}$$

$$C_{Crit} > \frac{I_{\text{Load}}}{f \times V_{\text{ripple}}} \tag{24}$$

where L_{Crit} and C_{Crit} were the minimum value of the inductor and capacitor to ensure the boost converter operated at continuous conduction mode (CCM). Although the CCM had disadvantages, i.e., needing a large inductor value, it offered advantages such as a lower ripple current, and the voltage gain was not influenced by the load. The low-power boost converter could start-up at least 800 mV [30]. Choosing the switching frequency of the boost converter was crucial. The following steps in designing the proposed EMS are:

- The boost converter 1 driven by MPPT IC SPV1040 was operated at a high frequency (100 kHz). It created a large *di/dt* which could pump the PV output current into the SC.
- The boost converter 2 driven by microcontroller dsPIC33FJGS502 was operated at a low frequency (2.5 kHz). A small *di/dt* prevented V_{SC} from dropping drastically because of an excessive SC discharge current.
- Because the input voltage that was given from the SC fluctuated, so the designing boost converter 2 must accommodate the wide-range input voltage. In this study, the input voltage had range around 1.2 to 5 V.
- On the other hand, the output voltage of the boost converter 2 had to be very tight to prevent fluctuation at the battery voltage. All parameters for experimental setup are listed in Tables 4–8.

Table 4. The SC parameters.

Items	Specification
Type	Electric Double Layer
Nominal Voltage/Capacity	9 V/1F
Internal Resistance	0.0350 ohm

Table 5. Battery parameters.

Items	Specification
Type	Lithium-Ion
Nominal Voltage/Capacity	7.4 V/0.7 Ah
Internal Resistance	0.0625 ohm

Table 6. Boost converter-1 parameters.

Items	Specification
Output Voltage	0.3–5 V
Input Voltage	0.3–5 V
Current Output (max)	0.5 A
L	15 uH
C	68 uH
Freq. switching/Max Duty Cycle	100 kHz/0.6

Table 7. Boost converter-2 parameters.

Items	Specification
Output Voltage	7.6–8.2 V
Input Voltage	1.2–5 V
Current Output (max)	1.5 A
L	1000 uH
C	68 uH
Freq. switching/Max Duty Cycle	2.5 kHz/0.3

Table 8. Solar panel parameters.

Items	Specification
Type	Monocrystalline IXOLAR SM531K10L
Open Circuit Voltage	6.91 V
Voltage/Current at maximum point	5.58 V/205 mA
Maximum peak power @ 1 panel	1.14 W
Configuration	4 parallel
Potential peak power	4.56 W

In Figure 14a, the microcontroller board for implementing PI-controller and data communication through LoRa communication module is shown. Figure 14b shows the board for two unidirectional boost converters, the SC and MPPT IC SPV1040. Software implementation was divided into two parts: (a) the PI-controller and data acquisition were embedded in the control board; (b) the FLC and data monitoring were implemented on the computer by using LabView.

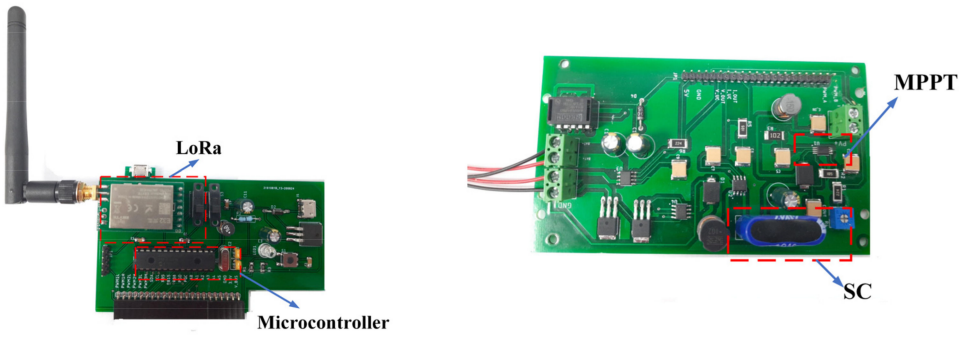

(**a**) (**b**)

Figure 14. The hardware of proposed EMS as: (**a**) controller board; (**b**) board for two unidirectional boost converters.

Figure 15 shows the flowchart that was embedded in the microcontroller dsPIC33FJGS502 control board. First, in making the initialization interrupt timer, serial communication module (i.e., Rx/Tx), interrupts Tx and PI-parameters. The PI-controller was located to interrupt the timer to obtain high-priority tasks and deterministic time sampling. Interrupting Tx brought

forth the second high-priority task to update $I^{*}_{SC\_ref}$, which was calculated by the FLC at the computer. In the infinite loop, only the mode selector was executed. The mode selector would check the battery voltage to prevent over-discharging. If the battery voltage is less than the minimum threshold, the switch T_1 starts to disconnect. Then the boost converter 2 starts to charge the battery and it is called hibernate mode.

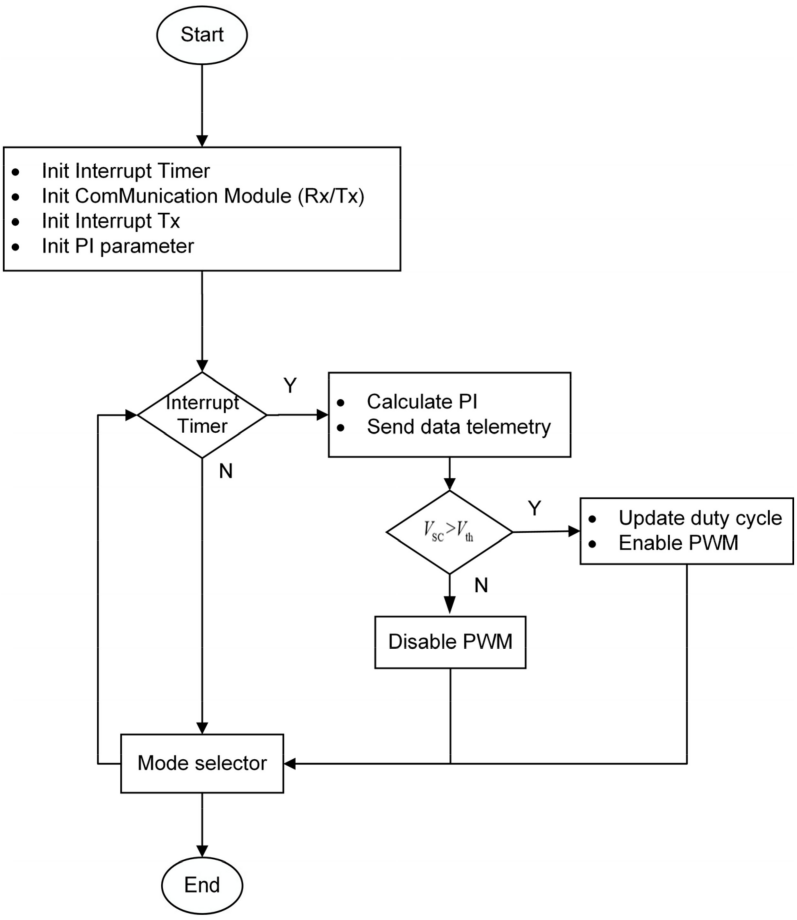

Figure 15. The flowchart of the PI-control scheme and data telemetry was implemented in the microcontroller.

When the interrupt timer happened, the PI-controller started to calculate the PWM register value. The value of PI-controller was limited such that it was not over from the maximum duty cycle. The PWM duty cycle register would be updated and enabled when V_{SC} is greater than V_{th}, otherwise the PWM register would be disabled until V_{SC} reaches V_{th}. This technique was adopted from [29], which used the burst mode switching pattern for dealing with very low input voltage.

Both FLC-1 and FLC-2 were implemented in LabView and a flowchart is shown in Figure 16. In the first stage, initialization PC port serial communication and loading the fuzzy inference system file occurred. In the next step, it waited for incoming data; if it did not receive new data, then buffer_serial_write was updated using the previous value. On the other hand, if it received new data, extracting an array string in V_{SC}, V_{Bat}, I_{SC}, and I_{Load}, then it was used to calculate FLC-1 and FLC-2. Output of FLC-1 and FLC-2 was employed to update buffer_serial_write and sent the data through LoRa module.

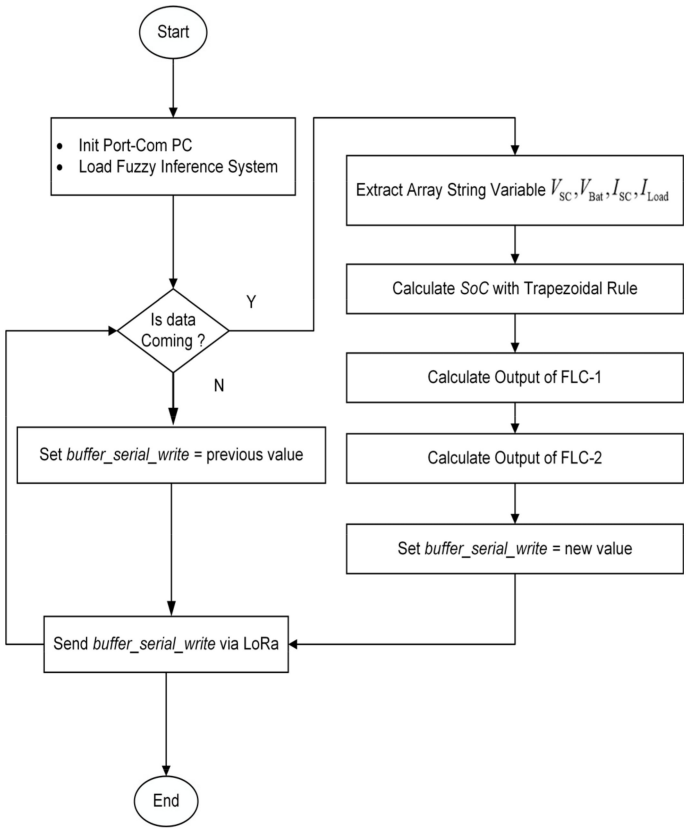

Figure 16. The flowchart of FLC-1 and FLC-2.

3. Results

Simulation and real experiment were employed for evaluating the proposed EMS performance. In the simulation part, it was tested with the static load and dynamic load. The V_{SC} would be evaluated by comparing with V_{SC_ref}. If it could stay not too far from V_{SC_ref}, it meant the proposed controller could work properly. The real experiment was only tested by constant load because of the limitation of laboratory equipment for generating the driving profile. Testing of three different values of V_{SC_ref} to obtain the best candidate was also conducted.

3.1. Simulation Result

The simulation and experiment were conducted to prove the effectiveness of the proposed EMS. In the first stage, the simulation was conducted by using SimPower MATLAB. Figure 17 shows the simulation using constant load. In this scenario, V_{SC_ref} equal to 2 V was used as threshold. When the V_{SC} was less than 2 V, the PWM generator was disabled and it waited to charge the SC until the V_{SC} reached threshold. The battery discharging current would be dropping when the SC started injecting its current. By keeping V_{SC} around V_{SC_ref}, the SoC_{SC} could be maintained around 19 to 21% as is shown in Figure 18. Although the I_{PV} was fluctuating, the V_{SC} could be kept very well at $\pm$2 V and it is presented in Figure 19. The goal to maintain the SoC_{SC} was satisfied by control scheme 1. To ensure the consistency of performance, a dynamic load test was conducted. Based on the result at Figure 20, the proposed EMS was still working to manage the I_{SC} when the I_{Load} was changed. Finally, Figure 21 shows that the V_{SC} was kept at maintenance, although the I_{PV} and I_{Load} were always fluctuating. This proved the robustness of the proposed EMS.

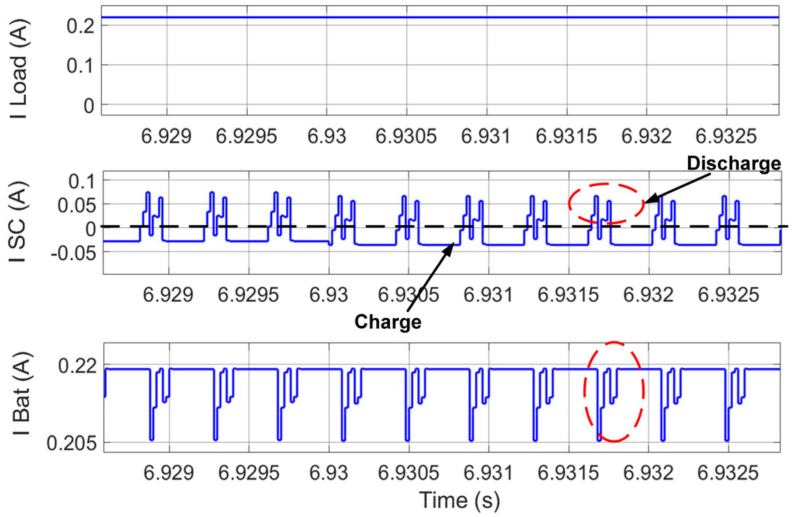

Figure 17. Current profile using a constant load.

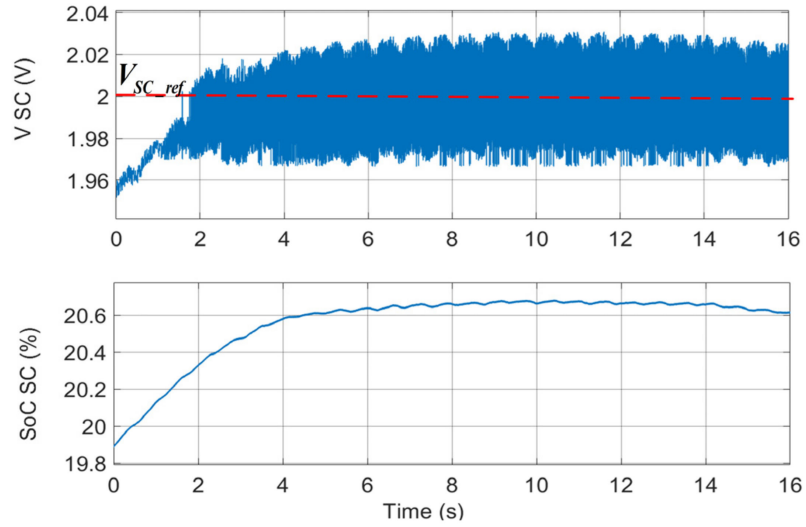

Figure 18. V_{SC} and SoC_{SC} relationship.

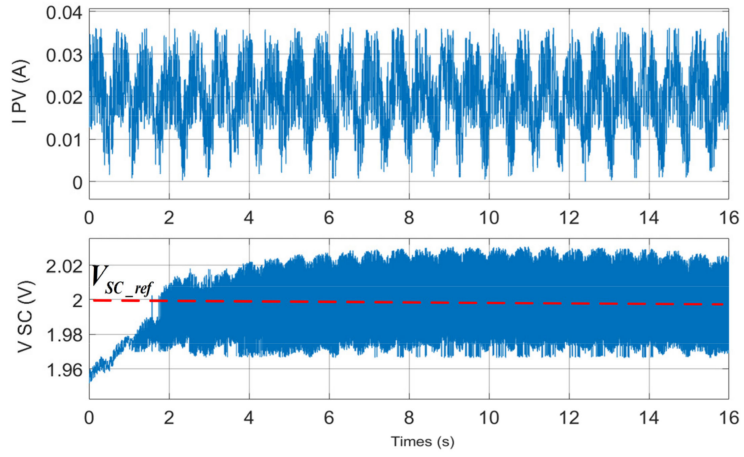

Figure 19. V_{SC} and I_{PV} when they were tested by a constant load.

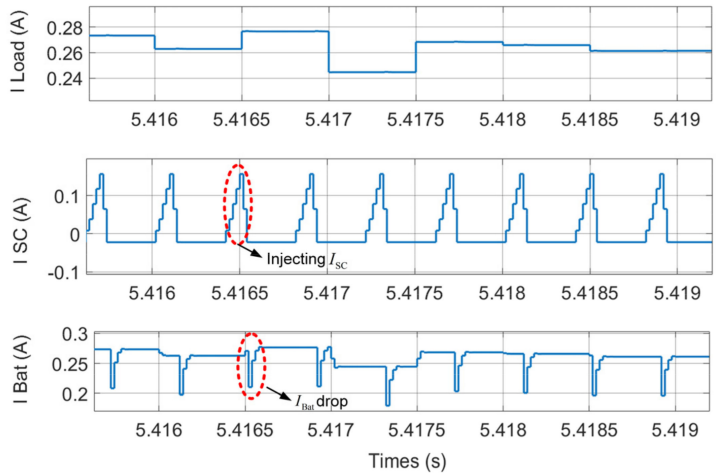

Figure 20. I_{SC} was tested by dynamic I_{Load}.

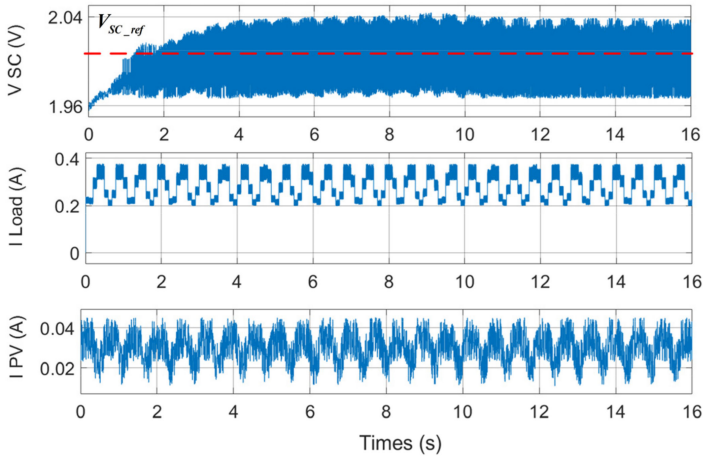

Figure 21. The V_{SC} stabilization when tested by dynamic I_{Load} and I_{PV}.

Figure 22 was called hibernate mode when the switch T_1 was off. In this condition, the load was not energized anymore and the PV current was used to charge the battery. The charging time duration was very dependent on I_{PV}; if the irradiance was not enough to generate sufficient power, then SoC_{Bat} would still be declining because the I_{PV} was lower than the EMS current consumption. This meant the EMS did not give a benefit when the I_{PV} was too low. By combining with control scheme 2 the I_{Load} could be adjusted based on the quantity of the existing PV current, as is illustrated in Figure 23. When the MA I_{PV} was dropping significantly, the FLC-2 also gave a response by reducing percentage P_{ref}, then the main controller would be making the decision to turn off some electronic module, so the current load would be declining.

3.2. Experimental Result

The experimental platform consists of LoRa module, proposed EMS, PV, and the load and it is displayed in Figure 24a, whereas the integration into MR is shown in Figure 24b. It is assumed that the RC-car, when adding some sensor, had a similar current consumption profile as MR. The load, i.e., DC motor and sensor, were used to discharge the battery and the data transmitted every 4.18 s through LoRa module.

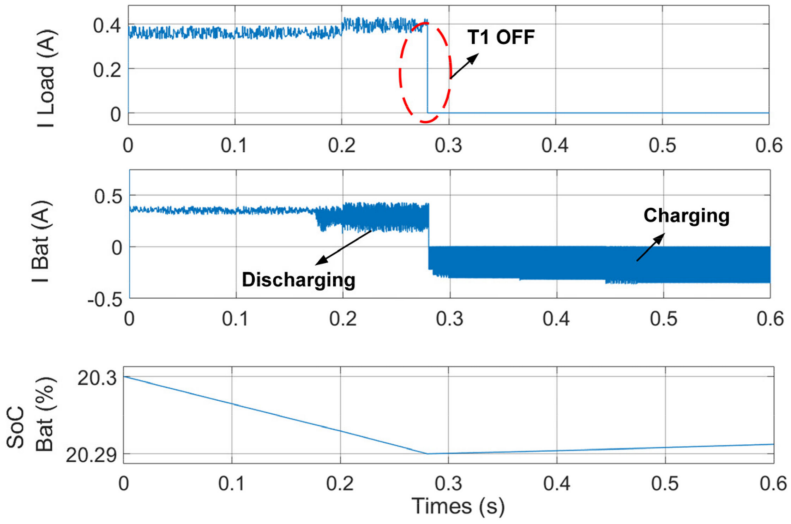

Figure 22. The hibernate mode.

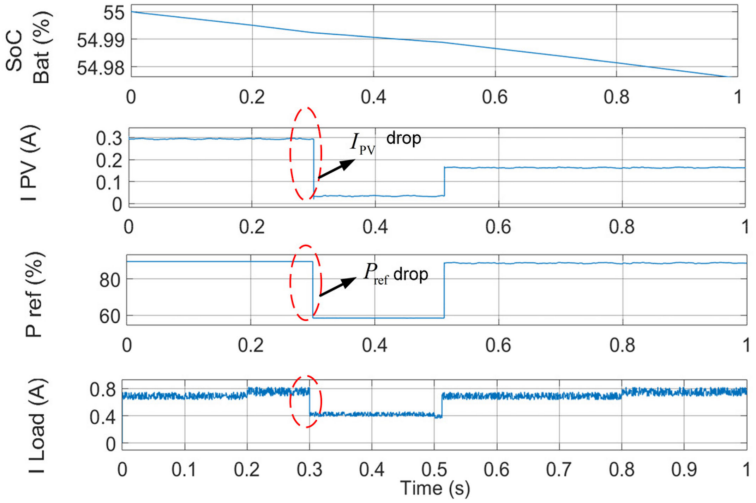

Figure 23. Integration with FLC-2.

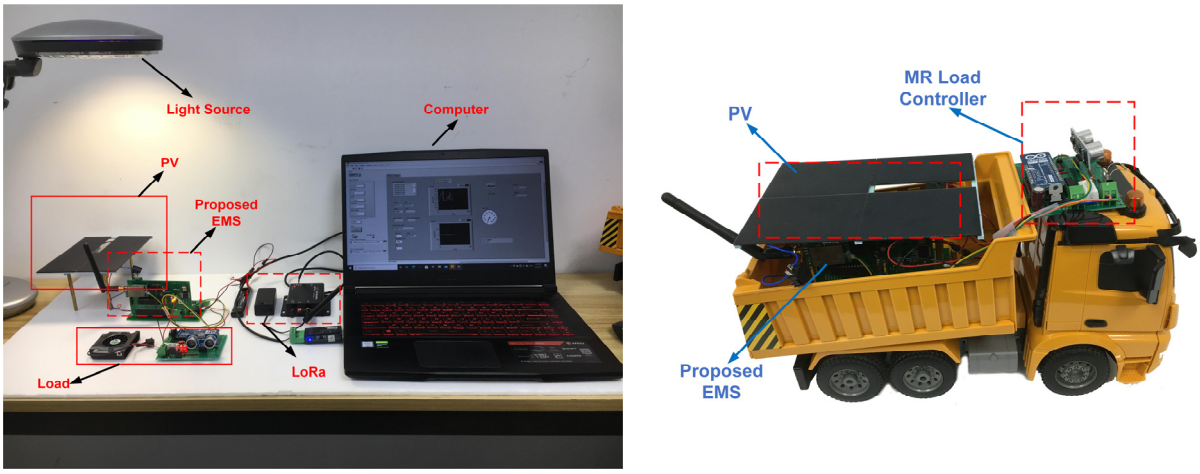

(**a**) (**b**)

Figure 24. Experimental platform: (**a**) using PV simulator; (**b**) integration into real MR.

There were three comparison performances, i.e., without EMS, with EMS-1, and with proposed EMS. The EMS-1 only used FLC-1 and PI-controller without applying the FLC-2 to determine the percentage of power reference. The result showed that the SoC_{Bat} was still higher around above 60%; there was no significant benefit by applying both EMS-1 or proposed EMS. This was because the PV energy that could be harvested was relatively small. However, after a certain time, the battery voltage without EMS started decreasing quickly, as is shown in Figure 25.

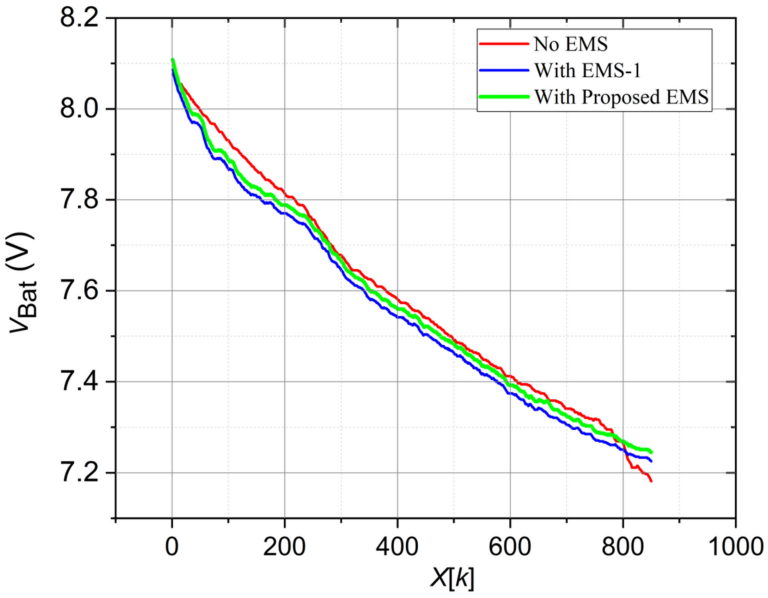

Figure 25. The battery voltage comparison.

The consequence of the battery voltage drop was that its ability to keep supplying constant current was declining. By applying the FLC-2, the main controller started to manage its load so it would reduce load current consumption drastically, as is shown in Figure 26.

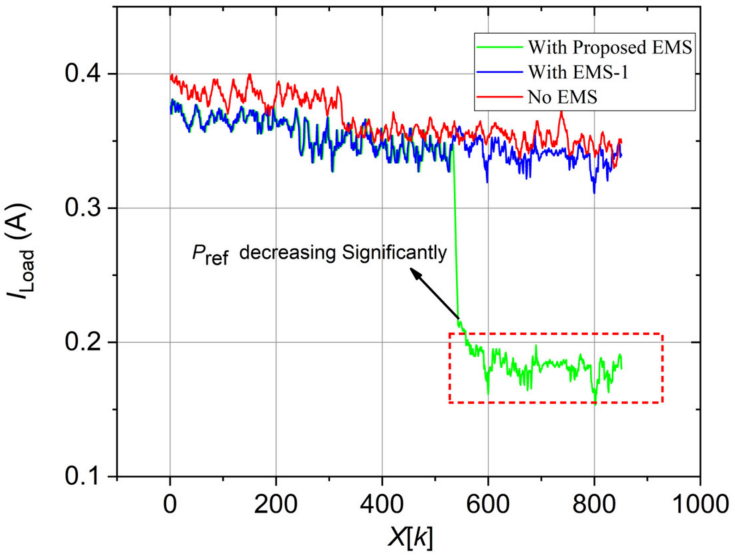

Figure 26. The load current consumption comparison.

In this case, the main controller turned off several sensors and kept the motor running. In the real case, the P_{ref} acted like a recommendation for the main controller to think about which electronic module it wanted to shut down in order to save the remaining battery

life. Because it was only a recommendation, not necessary to follow, so the result would be different for every case. Moreover, Figure 27 shows the power load distribution histogram, and it was clearly the load profile with proposed EMS having better performance. Managing the load as the main controller was doing had an important role in keeping the battery in safe operating condition because it was prevented from over-discharging. When the proposed EMS was applied, the battery current consumption would drop significantly, as is displayed in Figure 28.

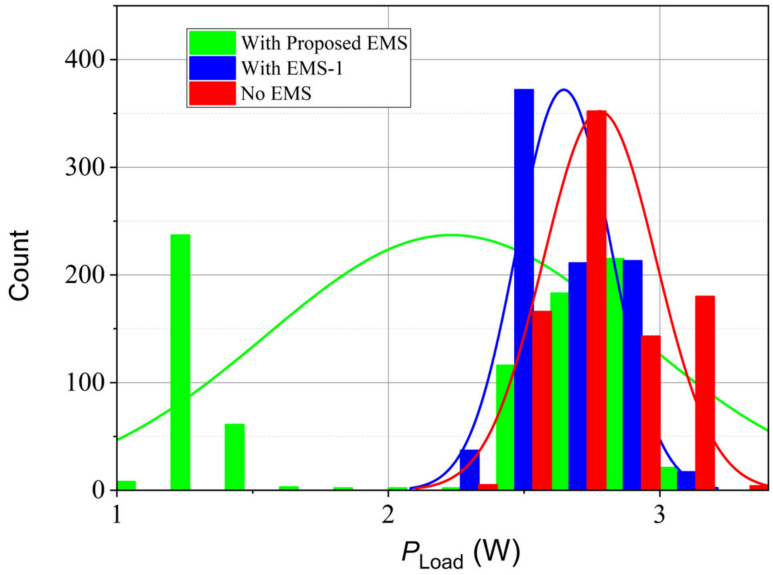

Figure 27. P_{Load} histogram comparison.

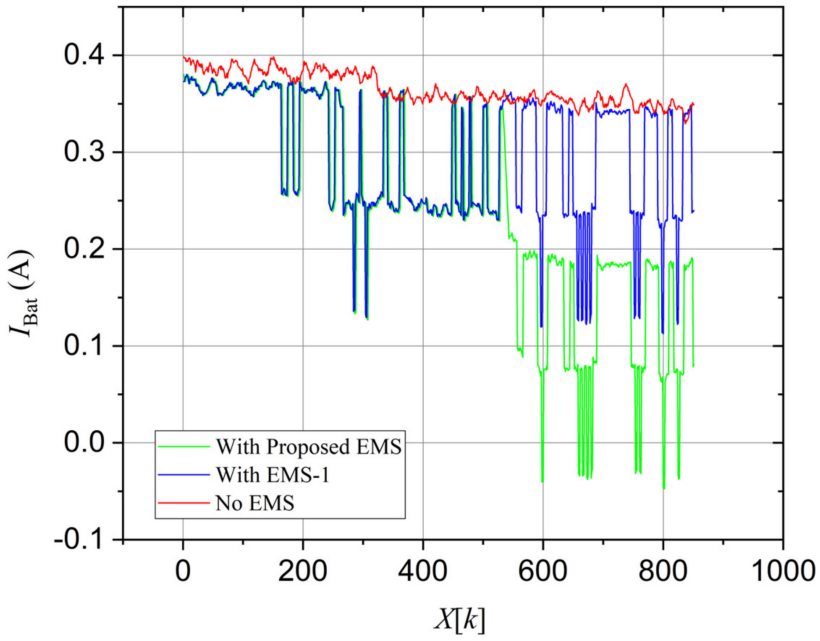

Figure 28. I_{Bat} consumption comparison.

The SoC estimation using trapezoidal rule-coulomb counting gave the result that the proposed EMS could save battery energy consumption. When the main controller reduced the load after receiving recommendation P_{ref}, it could significantly save energy, as is shown in Figure 29. Then, Figure 30 explains FLC-2 inference output surface to give the recommendation percentage of P_{ref}. Starting from SoC_{Bat} less than 80%, the system started giving recommendations by gradually reducing P_{ref}, but the main controller still

did not respond by reducing the power consumption because it was still a small value for the response. In the certain level of P_{ref}, the main controller started considering the P_{ref} recommendation.

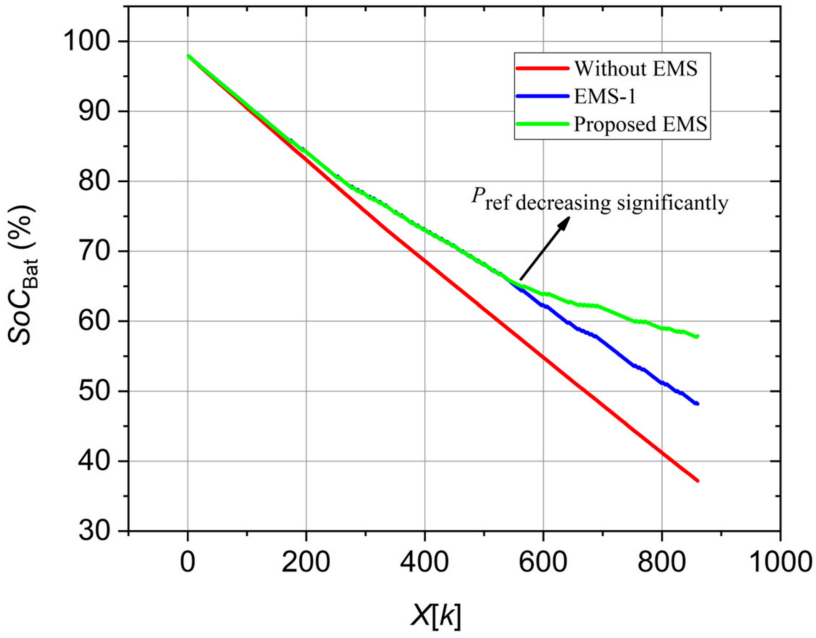

Figure 29. SOC_{Bat} comparison.

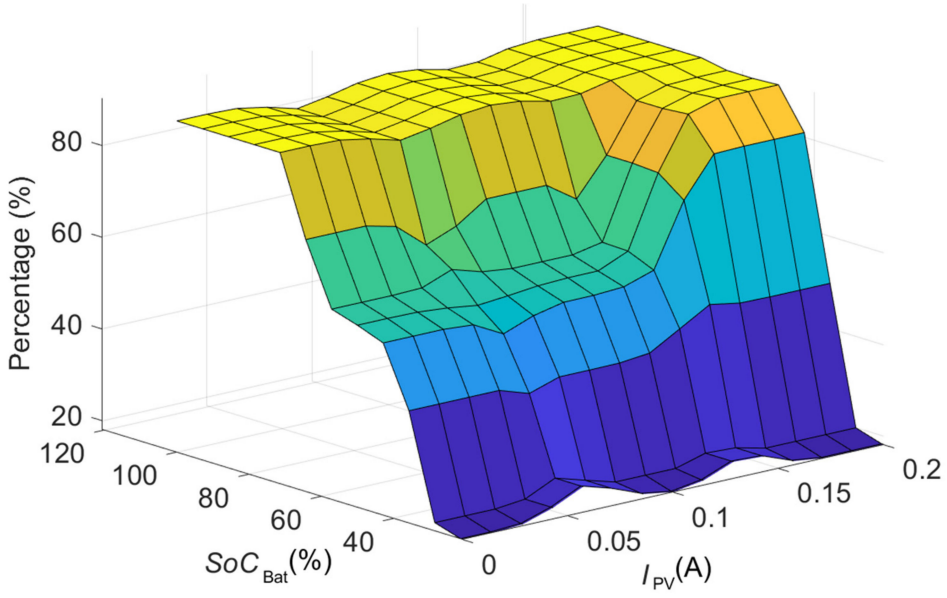

Figure 30. FLC-2 control surface.

All procedure related to load scheduling in the main controller was very subjective depending on the mission. The scope of our research did not cover issues relating to load scheduling/managing. How the proposed EMS could help the battery to reduce the peak battery discharge current is illustrated in Figure 31. When the SC started to discharge its current, some current flowed into the load and the rest was charged to the battery. In this experiment, current load I_{Load} around 0.38 A was used. When the SC started to inject its current, I_{Bat} consumption would be decreasing into minus value that indicated charging process, and at the same time, the V_{SC} would decline. After releasing I_{SC}, it started waiting to charge the SC such that V_{SC} reached around V_{SC_ref}. The ripple voltage V_{SC} in the real experiment was higher than that which occurred in simulation. The investigation found

that it was difficult to obtain precise PI-controller because most of the PI-controller was designed for the power converter majority based on the output voltage feedback, not based on the current input feedback. Another problem comes from the active current sensor that mostly exhibits less sensitivity with small ripple current ΔI_L that occurred in the inductor and led to a false feedback signal. Moreover, in the real experiment, to settle current in the low cell SC needed a longer time than in simulation. This caused the increasing time period to enable PWM, which often triggers a spike current. Based on Table 9, the proposed EMS could reduce the average battery current consumption until 35%, but it was very dependent on I_{PV} and how the central controller managed its load.

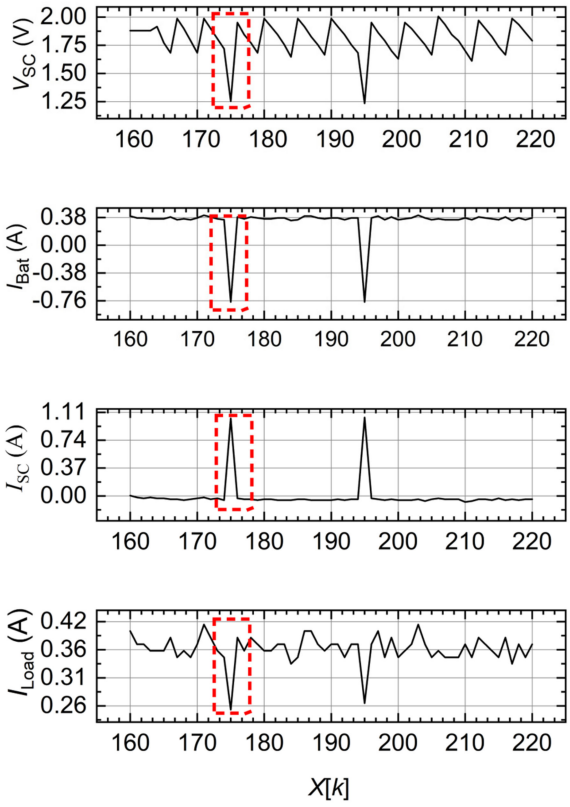

Figure 31. Injecting the SC current.

Table 9. Performances indicator.

Indicators	Prop-EMS	EMS-1	No-EMS
Max I_{Bat} (A)	0.38	0.38	0.40
Min I_{Bat} (A)	−0.05	0.11	0.33
Mean I_{Bat} (A) consumption	0.24	0.30	0.37
Standard Normal Distribution P_{Load} (W)	2.23	2.65	2.79
Final SoC_{Bat} (%)	57.88	48.20	37.20
Reducing I_{Bat} consumption (%)	35	18.92	-
Reducing peak I_{Bat} (%)	5	5	

On the other hand, if the EMS was running without combining with load management (EMS-1), it was only saving around 18%. Not only did it save the battery current consumption, it also reduced the battery peak current so it would increase the state of health of the battery. Figure 32 shows the response of the I_{SC} and V_{SC} with three differences, V_{SC_ref}. The lowest V_{SC_ref} produced the lowest SC discharge current (I_{SC}) with more frequent occurrences. Vice versa, the highest V_{SC_ref} produced the highest I_{SC} with less frequent occurrences. The I_{SC} with more frequent occurrences had significant benefits, i.e., reducing discharging current of the battery. However, too low I_{SC} was also not good for charging

the battery/hibernate mode because to charge the battery needed enough of the difference potential voltage between battery and output voltage of the boost converter-2. Table 10 shows comparison for the three differences, V_{SC_ref}. When the V_{SC_ref} was equal to 1.5 V, it had the best performance for the V_{SC} average voltage value and standard deviation but the I_{SC} average discharge current was the lowest. Based on a trade-off between the V_{SC} average voltage value and the I_{SC} average discharge current, the V_{SC_ref} equal to 1.78 V was one of the best options.

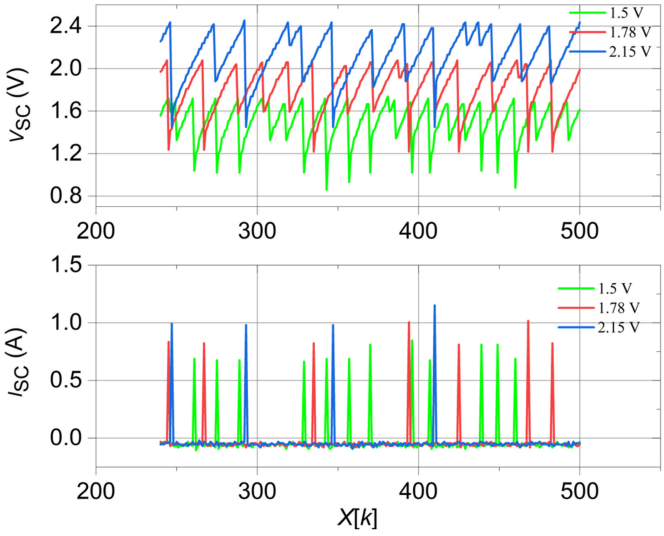

Figure 32. I_{SC} and V_{SC} with three differences V_{SC_ref}.

Table 10. The SC voltage reference.

Indicators	Value (V_{SC_ref})		
	1.5 V	1.78 V	2.15 V
Mean Voltage Value (V)	1.49	1.83	2.13
Standard Deviation	0.18	0.19	0.22
Max Value (V)	1.74	2.09	2.45
Min Value (V)	0.86	1.22	1.45
Peak to peak value (V)	0.88	0.87	1
Average Discharge Current (A)	0.83	1.01	1.18

4. Conclusions

The MR demand for SAR was increasing in accordance with the SAR task complexity. Every task had different time duration depending on scope, weather condition, and complexity. Furthermore, the ability to manage energy in the MR application offered sustainable operation. Most of the EMS designs conducted were not specifically designed for MR. By modification of the previous works such as modifications of the HESS topology and the control schemes, it offered specificity for the MR application.

It consisted of a PV/battery/SC that was regulated by the series path of a unidirectional boost converter. The semi-active type II HESS provided power-sharing between the SC and battery. By maintaining the SC voltage, it also maintained the SoC_{SC} at a certain level and then it gave sufficient space for the MPPT storing the PV energy. Two control schemes were proposed in this paper. The first control scheme was the combination of the FLC and PI-controller to manage power sharing i.e., by keeping the SC voltage. The FLC would give the SC discharge current reference to the PI-controller; it would keep the SC voltage at the certain value. The second control scheme also used another FLC to provide power reference recommendations to the central controller, as to how much percentage power load could be taken from the battery.

The simulation showed that the first control scheme could handle the constant and dynamic load test. The V_{SC} ripple voltage was very small and stable, although the I_{PV} and I_{Load} fluctuated. An unanticipated finding was that the real experiment yielded higher V_{SC} ripple voltage than the simulation result. The majority PI-controller for power converter was designed based on voltage feedback and failure to design the average current compensator led to oscillation. The most likely cause of the false feedback signal comes from the active current sensor that exhibits less sensitivity with small ripple current. Although it has some drawbacks, the experimental result concluded that it could save battery current consumption up to 35% and reduce the battery peak current up to 5%, depending on the existing I_{PV} and load management.

There are some suggestions to improve this project that are not covered in this work due to the limitation of resources and research time. The first recommendation is adding the average current compensator to improve the PI-controller performance. Moreover, combining the SC current and voltage as the feedback signal will increase resilience from noise. Secondly, the load management and scheduling shall be accommodated in the main controller to obtain a more efficient driving profile. Third, this project focuses on outdoor operations such as in fields or forests. In future work, adding fuel cells as backup power and giving special tasks to return to base when the battery starts to run out are needed. These measures are needed for special operations where there is no possibility to gather energy from the environment such as in small and dark environments (e.g., debris of collapsed buildings).

Every scenario robot in the real field had a unique load profile and different constraints, so it should be considered to design load management. Moreover, in order to reduce power consumption, the control scheme should be embedded in the main controller of the robot as one of the tasks, so it will drastically reduce power consumption because it does not need continuous communication with the PC host. The low-power single board computers (SBC) such as Nvidia Jetson are suitable as the main controller to execute the complex control scheme with minimum computation power consumption. Finally, the other renewable energy sources such as wind, heat, and vibration shall be explored to increase sustainability during the mission.

5. Patents

The patents resulting from the work reported in this manuscript are as follows: "Multiple Power Unmanned Aerial Vehicle", Patent No. TW I619643 B, Country: Taiwan, April 2018.

Author Contributions: Conceptualization, M.-F.R.L.; methodology, M.-F.R.L. and A.N.; software, A.N.; validation, M.-F.R.L. and A.N.; formal analysis, M.-F.R.L.; investigation, M.-F.R.L.; resources, M.-F.R.L.; data curation, A.N.; writing—original draft preparation, A.N.; writing—review and editing, M.-F.R.L.; visualization, A.N.; supervision, M.-F.R.L.; project administration, M.-F.R.L.; funding acquisition, M.-F.R.L. All authors have read and agreed to the published version of the manuscript.

Funding: This research was funded by Ministry of Science and Technology (MOST) in Taiwan, grant number [108-2221-E-011-142-] and Center for Cyber-physical System innovation from the Featured Areas Research Center Program within the framework of the Higher Education Sprout Project by the Ministry of Education (MOE) in Taiwan.

Institutional Review Board Statement: Not applicable.

Informed Consent Statement: Not applicable.

Data Availability Statement: Not applicable.

Conflicts of Interest: The authors declare no conflict of interest.

References

1. Nallathambi, D.J. Comprehensive evaluation of the performance of rescue robots using victim robots. In Proceedings of the 2018 4th International Conference on Control, Automation and Robotics (ICCAR), Auckland, New Zealand, 20–23 April 2018; pp. 60–64.
2. He, X.; Sun, X.; Wang, F.; Li, X.; Zhuo, F.; Luo, S. Design of energy management system for a small solar-powered unmanned aerial vehicle. In Proceedings of the 2018 9th IEEE International Symposium on Power Electronics for Distributed Generation Systems (PEDG), Charlotte, NC, USA, 25–28 June 2018; pp. 1–4.
3. Akar, F.; Tavlasoglu, Y.; Vural, B. An energy management strategy for a concept battery/ultracapacitor electric vehicle with improved battery life. *IEEE Trans. Transp. Electrif.* **2017**, *3*, 191–200. [CrossRef]
4. Shiau, J.; Ma, D.; Yang, P.; Wang, G.; Gong, J.H. Design of a solar power management system for an experimental uav. *IEEE Trans. Aerosp. Electron. Syst.* **2009**, *45*, 1350–1360. [CrossRef]
5. Alobeidli, K.; Khadkikar, V. A new ultracapacitor state of charge control concept to enhance battery lifespan of dual storage electric vehicles. *IEEE Trans. Veh. Technol.* **2018**, *67*, 10470–10481. [CrossRef]
6. Zhang, Q.; Li, G. Experimental study on a semi-active battery-supercapacitor hybrid energy storage system for electric vehicle application. *IEEE Trans. Power Electron.* **2020**, *35*, 1014–1021. [CrossRef]
7. Fu, Z.; Zhu, L.; Tao, F.; Si, P.; Sun, L. Optimization based energy management strategy for fuel cell/battery/ultracapacitor hybrid vehicle considering fuel economy and fuel cell lifespan. *Int. J. Hydrogen Energy* **2020**, *45*, 8875–8886. [CrossRef]
8. Ruiz-Cortés, M.; Romero-Cadaval, E.; Roncero-Clemente, C.; Barrero-González, F.; González-Romera, E. Energy management strategy to coordinate batteries and ultracapacitors of a hybrid energy storage system in a residential prosumer installation. In Proceedings of the 2017 International Young Engineers Forum (YEF-ECE), Almada, Portugal, 5 May 2017; pp. 30–35.
9. Liu, B.; Zhuo, F.; Zhu, Y.; Yi, H. System operation and energy management of a renewable energy-based dc micro-grid for high penetration depth application. *IEEE Trans. Smart Grid* **2015**, *6*, 1147–1155. [CrossRef]
10. Lee, B.; Kwon, S.; Park, P.; Kim, K. Active power management system for an unmanned aerial vehicle powered by solar cells, a fuel cell, and batteries. *IEEE Trans. Aerosp. Electron. Syst.* **2014**, *50*, 3167–3177. [CrossRef]
11. Avila, E.; Angélica, J.; Juan, C.; Marcelo, P.; Gabriel, B.; Paul, M.; Andrés, P.; Nilo, O.; Vicente, C.; Alejandro, V. Energy management of a solar-battery powered fixed-wing uav. In Proceedings of the 2018 International Conference on Information Systems and Computer Science (INCISCOS), Quito, Ecuador, 13–15 November 2018; pp. 180–185.
12. Cong, D.; Yan, X.; Chen, J. A program about power management system for service robot. In Proceedings of the 2017 29th Chinese Control and Decision Conference (CCDC), Chongqing, China, 28–30 May 2017; pp. 4912–4915. [CrossRef]
13. Adrian, L.R.; Ribickis, L. Proposed piezoelectric energy harvesting in mobile robotic devices. In Proceedings of the 2014 55th International Scientific Conference on Power and Electrical Engineering of Riga Technical University (RTUCON), Riga, Latvia, 14 October 2014; pp. 63–66.
14. Armenta, J.; Núñez, C.; Visairo, N.; Lázaro, I. An advanced energy management system for controlling the ultracapacitor discharge and improving the electric vehicle range. *J. Power Sources* **2015**, *284*, 452–458. [CrossRef]
15. Wang, B.; Xu, J.; Cao, B.; Zhou, X. A novel multimode hybrid energy storage system and its energy management strategy for electric vehicles. *J. Power Sources* **2015**, *281*, 432–443. [CrossRef]
16. Yin, H.; Zhou, W.; Li, M.; Ma, C.; Zhao, C. An adaptive fuzzy logic-based energy management strategy on battery/ultracapacitor hybrid electric vehicles. *IEEE Trans. Transp. Electrif.* **2016**, *2*, 300–311. [CrossRef]
17. Marzougui, H.; Kadri, A.; Martin, J.-P.; Amari, M.; Pierfederici, S.; Bacha, F. Implementation of energy management strategy of hybrid power source for electrical vehicle. *Energy Convers. Manag.* **2019**, *195*, 830–843. [CrossRef]
18. Florescu, A.; Bacha, S.; Munteanu, I.; Bratcu, A.I.; Rumeau, A. Adaptive frequency-separation-based energy management system for electric vehicles. *J. Power Sources* **2015**, *280*, 410–421. [CrossRef]
19. Hredzak, B.; Agelidis, V.G.; Jang, M. A Model Predictive Control System for a Hybrid Battery-Ultracapacitor Power Source. *IEEE Trans. Power Electron.* **2014**, *29*, 1469–1479. [CrossRef]
20. Moreno, J.; Ortuzar, M.E.; Dixon, J.W. Energy-management system for a hybrid electric vehicle, using ultracapacitors and neural networks. *IEEE Trans. Ind. Electron.* **2006**, *53*, 614–623. [CrossRef]
21. Covaci, C.; Gontean, A. Piezoelectric energy harvesting solutions: A review. *Sensors* **2020**, *20*, 3512. [CrossRef] [PubMed]
22. Ünlü, M.; Çamur, S. A simple photovoltaic simulator based on a one-diode equivalent circuit model. In Proceedings of the 2017 4th International Conference on Electrical and Electronic Engineering (ICEEE), Ankara, Turkey, 8–10 April 2017; pp. 33–36.
23. Cabrane, Z.; Ouassaid, M.; Maaroufi, M. Management and control of the integration of supercapacitor in photovoltaic energy storage. In Proceedings of the 2017 International Conference on Green Energy Conversion Systems (GECS), Hammamet, Tunisia, 23–25 March 2017; pp. 1–6.
24. Bi, K.; Sun, L.; An, Q.; Duan, J. Active soc balancing control strategy for modular multilevel super capacitor energy storage system. *IEEE Trans. Power Electron.* **2019**, *34*, 4981–4992. [CrossRef]
25. Argyrou, M.C.; Christodoulides, P.; Marouchos, C.C.; Kalogirou, S.A. Hybrid battery-supercapacitor mathematical modeling for pv application using matlab/Simulink. In Proceedings of the 2018 53rd International Universities Power Engineering Conference (UPEC), Glasgow, UK, 4–7 September 2018; pp. 1–6.
26. Islam, S.M.R.; Park, S.; Balasingam, B. Circuit parameters extraction algorithm for a lithium-ion battery charging system incorporated with electrochemical impedance spectroscopy. In Proceedings of the 2018 IEEE Applied Power Electronics Conference and Exposition (APEC), San Antonio, TX, USA, 4–8 March 2018; pp. 3353–3358.

27. Nugroho, A.; Rijanto, E.; Wijaya, F.D.; Nugroho, P. Battery state of charge estimation by using a combination of coulomb counting and dynamic model with adjusted gain. In Proceedings of the 2015 International Conference on Sustainable Energy Engineering and Application (ICSEEA), Bandung, Indonesia, 5–7 October 2015; pp. 54–58.
28. Boni, E.; Montagni, M.; Moreschi, A.; Pugi, L. Energy Storage System optimization for an Autonomous Sail Boat. In Proceedings of the 2019 IEEE 5th International Forum on Research and Technology for Society and Industry (RTSI), Florence, Italy, 9–12 September 2019; pp. 231–235. [CrossRef]
29. Ogawa, T.; Ueno, T.; Miyazaki, T.; Itakura, T. 20 mV input, 4.2 V output boost converter with methodology of maximum output power for thermoelectric energy harvesting. In Proceedings of the 2016 IEEE Applied Power Electronics Conference and Exposition (APEC), Long Beach, CA, USA, 20–24 March 2016; pp. 1907–1910.
30. Meehan, A.; Gao, H.; Lewandowski, Z. Energy harvest with microbial fuel cell and power management system. In Proceedings of the 2009 IEEE Energy Conversion Congress and Exposition, San Jose, CA, USA, 20–24 September 2009; pp. 3558–3563.